pp. 1–21 (2024)

Temporally and spatially segregated discretization for a coupled electromechanical myocardium model

A. A. Danilov[abcde], A. A. Liogky[*abcf], and F. A. Syomin[a]

Abstract — In this paper, we propose a novel temporally and spatially segregated numerical scheme to discretize the coupled electromechanical model of myocardium. We perform several numerical experiments with activation of a myocardial slab with structural inhomogeneity and evaluate the dependence of numerical errors on the size of spatial and temporal discretization steps. In our study, we show that the spatial step for the mechanical equations $h_m \leqslant 2.5$ mm yields reasonable results with noticeable errors only in the region of myocardial inhomogeneity. We also show that time step $\tau_m \leqslant 1$ ms can be used for temporal discretization of mechanical equations, and the propagation velocity of the activation and contraction fronts differs from the reference one by no more than 1.3% for such time step. Finally, we show that the increase of time discretization steps of the mechanical equations τ_m and the monodomain equation τ_e leads to phase errors with opposite signs, and we can compensate these errors by tuning the relationship between the time steps.

Keywords: Mathematical modelling, multiscale models, cardiac electromechanics, high performance computing, multiphysics problems, numerical simulation, finite element method

MSC 2010: 65M60, 74F99, 74S05

In recent years, mathematical modelling has been increasingly used in various fields of medicine and, in particular, in cardiology. Actively developing models of cardiac electromechanics are promising tools for simplifying clinical decision-making, providing personalization in treatment approaches and obtaining new knowledge about various diseases and possible methods for their diagnosis and treatment. For example, mathematical models are used to evaluate the effectiveness of anti-arrhythmic drugs and defibrillation methods [7, 14, 21, 34, 35], studies of ischemia, hypertension and other diseases [2, 5, 17, 28, 37].

The coupled cardiac electromechanics model usually includes the following submodels: cellular active tension generation equations, cellular ionic equations, fi-

[a]Institute of Mechanics, Lomonosov Moscow State University, Moscow 119192
[b]Marchuk Institute of Numerical Mathematics of the RAS, Moscow 119333
[c]Sirius University of Science and Technology, Sochi 354340
[d]Institute of Computer Science and Mathematical Modeling, Sechenov First Moscow State Medical University, Moscow 119991
[e]Moscow Institute of Physics and Technology, Dolgoprudny 141701
[f]World-Class Research Center 'Digital biodesign and personalized healthcare', Sechenov First Moscow State Medical University, Moscow 119991
[*] E-mail: al.liogky@yandex.ru

The study was performed at the Institute of Mechanics, Lomonosov Moscow State University, and supported by the Russian Science Foundation project No. 22-71-10007.

nite strain mechanical equations, and equations of electrical activation propagation. Importantly, each of these submodels has its own strongly different characteristic spatial and temporal scales. Therefore, an extremely promising approach is the utilization of fully segregated numerical schemes, i.e., schemes that allow to use the different time steps and even different spatial discretizations for modelling of individual subprocesses. Several variants of segregated schemes have been previously proposed to solve the cardiac electromechanical problems [3, 6, 8, 24, 27]. In our scheme we couple electrical and mechanical parts through the state variables at the integration points. The general idea behind this approach is not new [11, 18, 19, 26]. However, most works are based on discretization of space on a common mesh or structured hierarchical meshes, require some interpolation procedures, and/or have other limitations. In this paper we propose a novel numerical scheme to discretize the coupled cardiac electromechanics model, which differs from the previously proposed schemes in lifting requirement for certain consistency between the meshes used for discretizations of the mechanics equations and the equations of electrical activation propagation, as well as for utilization of unstructured tetrahedral rather than hexahedral meshes. Our numerical scheme does not use interpolations from one mesh to another, though some minor extra computations may be required in one part of the model if the other part of the model uses a different computational mesh.

In any numerical simulations, numerical errors are inevitable, and if their magnitude is large enough, they can lead to misinterpretation of the obtained solutions. On the other hand, in practical calculations we are always limited in time and computational resources. As a result, it is necessary to search for a balance between the accuracy of the obtained solution and the resources spent for obtaining this solution. That is why, when using the model, it is necessary to investigate what scale of computational errors occur in the model depending on the fineness of the discretizations used. In this paper, we apply our numerical scheme to discretize the coupled electromechanics model of the myocardium slab from the previous work [32]. The numerical experiments performed within the CarNum cardiac modelling framework [15] give us the estimates for spatial and time discretization steps for the mechanical equations and the monodomain equation needed for a reasonable accuracy. Since the model considered in our study uses rather simple variants of individual submodels, such as the Aliev–Panfilov model for ionic equations, the Fung-type isotropic material to describe passive mechanical properties, the monodomain equation to model activation propagation, etc., it is likely that for more complex models the restrictions on the discretization steps will be more stringent, but the estimates presented in this study can still be used as a priori knowledge of the existing restrictions.

In Section 1 we give a brief mathematical formulation of the coupled electromechanical model. Next, in Section 2, we provide a detailed description of our proposed numerical scheme for the discretization of this model. And finally, in Section 3 we present the results of numerical experiments and analyze the discretization errors that occur when using the proposed scheme.

1. Mathematical models of myocardial electromechanics

We consider a coupled model of cardiac electromechanics consisting of four interconnected submodels: cardiac electrical propagation, continuum mechanics, cell active contraction and cell-membrane electrophysiology. We denote the considered piece of myocardium in an initial undeformed configuration by Ω, and we introduce the following notations for the model variables: $\mathbf{u} : \Omega \to \mathbb{R}^3$ is the mechanical displacement field of the tissue, $v : \Omega \to \mathbb{R}$ is the transmembrane potential, $\mathbf{w} : \Omega \to \mathbb{R}^{n_w}$ are state variables of cellular electrophysiology model, and $\mathbf{a} : \Omega \to \mathbb{R}^{n_a}$ are state variables for model of cardiomyocyte contraction and its activation.

1.1. Monodomain equation

We use a monodomain model [25] as a model of electrical propagation, which in the initial configuration reads as follows:

$$C_m \frac{\partial v}{\partial t} - \nabla \cdot (\sigma \nabla v) + i_{\text{ion}}(v, \mathbf{w}) = i_{\text{stim}}(t), \quad \mathbf{X} \in \Omega$$

with an insulating boundary condition

$$(\sigma \nabla v) \cdot \mathbf{N} = 0, \quad \mathbf{X} \in \partial\Omega.$$

Here σ is the conductivity tensor given by

$$\sigma = \sigma_{\text{iso}}\, \mathbb{I} + \sigma_{\text{aniso}}\, \mathbf{f} \otimes \mathbf{f}$$

variation of the normalized membrane capacitance C_m depends on the fibers strain upon their stretch to account for the mechano-electrical feedback and is described by the equation [32]:

$$\frac{\partial C_m}{\partial t} = k_m(K_m(\lambda_f - 1)_+ - (C_m - 1)), \quad \mathbf{X} \in \Omega$$

the transmembrane ionic current i_{ion} is specified by an ionic model, i_{stim} is an external stimulation, $(x)_+ = (|x| + x)/2$, $\lambda_f = \sqrt{(\mathbb{F}\mathbf{f}, \mathbb{F}\mathbf{f})}$ is the fiber stretch with deformation gradient $\mathbb{F} = \mathbb{I} + \nabla \mathbf{u}$ and fiber direction $\mathbf{f}$, $\|\mathbf{f}\| = 1$.

For simplicity, we will further move the last ordinary differential equation (ODE) to the system of the ODEs of cell-level electrophysiology and also assume C_m is a component of $\mathbf{w}$.

1.2. Membrane ionic model

We couple the monodomain equation with the Aliev–Panfilov (AP) ionic model [1] given by

$$\tau \frac{\partial v}{\partial t} = -\left(\varepsilon + \frac{\mu_1 v}{\mu_2 + u}\right)(v + ku(u - a - 1)), \quad \mathbf{X} \in \Omega$$

which includes the nondimensional membrane potential $u = (v - V_{\text{min}})/V_{\text{norm}}$, $\nu \in \mathbf{w}$ is the ionic state variable, the ionic current

$$i_{\text{ion}}(u,\nu) = \frac{uV_{\text{norm}}}{\tau}\left((1+k_{i1})\nu + k(u-(1+k_{i2})a)(u-1) \right)$$

as well as parameters ε, μ_1, μ_2, k, a, τ, V_{min}, V_{norm}. Also here we introduce two additional parameters k_{i1} and k_{i2}, which will be used in numerical experiments to simulate the heterogeneity of the material.

1.3. Continuum mechanical model

We describe the mechanical behaviour of the myocardium using the classical momentum balance equation which reads as follows:

$$\rho \frac{\partial^2 \mathbf{u}^i}{\partial t^2} - \sum_{j=1}^{3} \nabla_j \mathbb{P}^{ij} = 0, \qquad i \in \{1,2,3\}, \quad \mathbf{X} \in \Omega$$

where ρ is a tissue density in the initial configuration, $\mathbf{u}^i$ is the i-th component of $\mathbf{u}$, and $\mathbb{P}$ is the first Piola-Kirchhoff stress tensor. This equation is supplemented by boundary conditions

$$\mathbb{P}\mathbf{N} + (k_{\parallel}\mathbf{N}\otimes\mathbf{N} + k_{\perp}(\mathbb{I} - \mathbf{N}\otimes\mathbf{N}))(\mathbf{u} - \mathbf{u}_{\text{spr}}) = -p_{\text{ext}} J \mathbb{F}^{-T}\mathbf{N}, \quad \mathbf{X} \in \partial\Omega$$

where $k_{\parallel} \geqslant 0$ and $k_{\perp} \geqslant 0$ are normal and tangential spring mounting stiffnesses relative to a relaxed state $\mathbf{u}_{\text{spr}}$, respectively, p_{ext} is an external pressure on the boundary, $\mathbb{F} = \mathbb{I} + \nabla\mathbf{u}$, and $J = \det \mathbb{F}$.

Assuming the incompressibility of myocardial tissue and using the active stress approach [22], we have the following decomposition:

$$\mathbb{P} = \mathbb{P}_{\text{pas}} + \mathbb{P}_{\text{vol}} + \mathbb{P}_{\text{cell}}$$

where the terms represent passive stress, near-incompressibility volumetric penalty and cell-level stress including active stress, respectively. The first two terms are given using scalar hyperelastic potentials as

$$\mathbb{P}_{\text{type}} = \frac{\partial W_{\text{type}}(\mathbb{F})}{\partial \mathbb{F}}, \quad \text{type} \in \{\text{pas},\ \text{vol}\}.$$

To describe the passive properties of the myocardium, the isochoric variant of the Fung-type isotropic material [9] is considered

$$W_{\text{pas}} = \frac{\mu}{2}\left(\exp\left(b\ \text{tr}(\widehat{\mathbb{E}}^2)\right) - 1\right)$$

and the volumetric term is given by

$$W_{\text{vol}} = \frac{K}{4}(J^2 - 1 - 2\ln J))$$

where $\widehat{\mathbb{E}} = \frac{1}{2}(J^{-2/3}\mathbb{F}^T\mathbb{F} - \mathbb{I})$ is the isochoric variant of the Green–Lagrange strain tensor and μ, b, K are model parameters. In turn, the active stress acts only along fibers and has the form:

$$\mathbb{P}_{\text{cell}} = T_{\text{cell}}(\lambda_f,\ \partial_t\lambda_f,\ \mathbf{a})\ \frac{\mathbb{F}\mathbf{f}\otimes\mathbf{f}}{\lambda_f}$$

where $\lambda_f = \sqrt{(\mathbb{F}\mathbf{f}, \mathbb{F}\mathbf{f})}$ is the relative fiber stretch and $\partial_t\lambda_f = \partial\lambda_f/\partial t$ is the fiber stretch-rate.

1.4. Cellular active tension generation

In this work, we took into account two cell-level stress variables: passive nonlinear-elastic reaction of sarcomeric protein titin to strain T_{tit} and the active stress T_{act} developed by contractile proteins myosin and actin due to Ca^{2+} activation of their interaction and other mechano-chemical processes in muscle:

$$T_{\text{cell}} = T_{\text{tit}} + T_{\text{act}}.$$

The titin stress was initially set by the expression for a long protein chain (worm-like chain model) adapted from [16]. In this study, we use its approximation by an exponential polynomial of λ_f:

$$T_{\text{tit}} = t_{\text{tit}}\varepsilon_\lambda \cdot \begin{cases} \exp(q_1\varepsilon_\lambda + q_2\varepsilon_\lambda^2 + q_3\varepsilon_\lambda^3), & \varepsilon_\lambda > 0 \\ \exp(q_1\varepsilon_\lambda + q_2^*\varepsilon_\lambda^2), & \text{otherwise,} \end{cases} \qquad \varepsilon_\lambda = \lambda_f - 1.$$

The coefficients here (see Table 2 for actual values) were set from fitting the tension-strain curves for stretched sarcomers to simulation results in study [30], in which the worm-like chain model [16] was used. The approximation allowed us to get rid of the denominator that may approach zero during the solution of a nonlinear system for macromechanics (motion equations and, potentially, incompressibility equations). Moreover, though we could not find any reliable data on titin reaction to shortening, we made the titin in our model stiff enough at $\lambda_f < 1$ to avoid very short sarcomere lengths at which the filaments would be damaged.

The cell-level active stress model is described by the computationally efficient Syomin–Osepyan–Tsaturyan model [31]:

$$\begin{cases} T_{\text{act}} = T_{\text{act}}(\lambda_f,\ \partial_t\lambda_f,\ \mathbf{a}) \\ \dfrac{\partial\mathbf{a}}{\partial t} = \mathbf{r}_{\mathbf{a}}(\lambda_f,\ \partial_t\lambda_f,\ v,\ \mathbf{a}), \quad \mathbf{X}\in\Omega. \end{cases}$$

The active tension in the cardiomyocyte model used in this study depends on a number of cross-bridges formed by sarcomeric contractile proteins (n), the ensemble-average displacement of cross-bridges in sarcomere δ, the fraction of the cross-bridges being in strongly-bound force generated state (ϑ) accompanied by

their average displacement h, and the overlap zone of the contractile filaments W, which is piecewise linear function of the sarcomere strain. Explicitly, we choose W as a function proposed in [29]:

$$W(\lambda_f) = \begin{cases} 0, & l_s \leqslant l_0 \\ \frac{l_s - l_0}{l_m + 2l_z - l_0} W_0, & l_0 < l_s \leqslant l_m + 2l_z \\ W_0 + (1 - W_0)\frac{l_s - l_m - 2l_z}{2l_a - l_b - l_m - 2l_z}, & l_m + 2l_z < l_s \leqslant 2l_a - l_b \\ 1, & 2l_a - l_b < l_s \leqslant 2l_a + l_b \\ 1 - \frac{l_s - 2l_a - l_b}{l_m - l_b}, & 2l_a + l_b < l_s \leqslant l_m + 2l_a \\ 0, & l_s > l_m + 2l_a \end{cases}$$

where $W_0 = 2(l_m + l_z - l_a)/(l_m - l_b)$, $l_s = \lambda_f l_{s0}$.

The constitutive equation for the active stress, with dimensionless δ (after division by h) reads

$$T_{\text{act}} = p_{f1} E N_m N_{xb} h n W(\lambda_f) \cdot (\delta + \vartheta).$$

For meanings and values of other parameters we refer to [31]. The variables stated above belong to the set **a** of cell-level variables, which also includes concentrations of activated regulatory proteins, calcium concentrations in different compartments of a cell, and some other variables required for the specification of electromechanical coupling. Here we focus only on the kinetic equations for contractile proteins, as we use those to specify the approximation of δ, which make our numerical scheme much more stable. The variables n and ϑ are defined by kinetic equations

$$\begin{aligned} \frac{\partial n}{\partial t} &= k_{\text{cb}} \left(k_{01} \left(A_1^2 - n \right) - k_{10} n \right) \\ \frac{(\partial n \vartheta)}{\partial t} &= k_{\text{cb}} \left(k_{12} n \cdot (1 - \vartheta) - k_{21} n \vartheta \right) \end{aligned}$$

where k_{cb} is a characteristic rate of the cross-bridges kinetics, A_1 is the concentration of regulatory complexes activated by Ca^{2+} ions in the overlap zone of the contractile filaments (where the complexes affect cross-bridges binding sites), and k_{ij} are nondimensional kinetic rates for the corresponding transitions. The rates depend on δ except for k_{21}, which is constant, and $k_{12} = k_{21} \mathrm{e}^{-\gamma\delta}$. Kinetic rates k_{01} and k_{10} are defined as follows

$$k_{01} = \begin{cases} 1, & \delta \leqslant 0 \\ \frac{\delta_2^{*2}}{\left(\delta_2^* - \delta\right)^2}, & \delta > 0, \end{cases} \qquad k_{10} = \begin{cases} a_{10} + b_{10}\delta^2, & \delta \leqslant 0 \\ a_{10} + \frac{\delta}{\delta_2^* - \delta}, & \delta > 0. \end{cases}$$

Meanwhile, the variation of δ depends on the rate of the sarcomeric strain ($l_{s0}\lambda_f$ in our setup) and the rates of the cross-bridges kinetics, as their attachment and detachment change an average cross-bridge displacement:

$$\frac{(\partial n \delta)}{\partial t} = \frac{n l_{s0}}{2h} \frac{\partial \lambda_f}{\partial t} - k_{cb} k_{10} n \delta$$

or

$$\frac{\partial \delta}{\partial t} = \frac{l_{s0}}{2h}\frac{\partial \lambda_f}{\partial t} - \frac{k_{cb}k_{01}(A_1^2-1)\delta}{n}.$$

One can notice that the variation of δ is strongly coupled with mechanics through the strain rate, while the active stress T_{act} depends on δ explicitly. It was shown earlier [23] that the application of a segregated scheme, i. e., the usage of the δ value from the previous time step in T_{act} for assembling Jacobian matrix for the system of nonlinear equations for mechanics, resulted in a poor convergence of the numerical solver. We found out that the scheme becomes stable if we assume that the muscle contraction is a steady-state process at every single time step of discretized motion equations. Thus, we can replace δ in T_{act} with its stationary counterpart δ_{stat}. From stationary equations for n and δ we derive a quadratic or cubic equation for δ depending on the strain

$$0 = \beta - k_{10}\delta$$

where

$$\beta = \frac{l_{s0}}{2hk_{cb}}\frac{\partial \lambda_f}{\partial t}$$

is nondimensional contraction velocity expressed in terms of degrees of freedom of displacement field $\mathbf{u}$. We note that β is constant at every time step of our segregated scheme.

The expression for δ_{stat} values is

$$\delta_{\text{stat}} = \begin{cases} \sqrt[3]{\dfrac{\sqrt{81\beta^2+12a_{10}^3/b_{10}}+9\beta}{18b_{10}}} - \dfrac{2a_{10}}{\sqrt[3]{12b_{10}^2(\sqrt{81\beta^2+12a_{10}^3/b_{10}}+9\beta)}}, & \beta \leqslant 0 \\ \dfrac{\beta + a_{10}\delta^*}{2(a_{10}-1)}\left(1 - \sqrt{1 - \dfrac{4\beta\delta^*(a_{10}-1)}{(\beta+a_{10}\delta^*)^2}}\right), & 0 < \beta \leqslant \beta^* \\ \delta_2^*, \quad \beta > \beta^* \end{cases}$$

$$\beta^* = \delta_2^*\left(a_{10} + \frac{\delta_2^*}{\delta^* - \delta_2^*}\right)$$

where β^* and δ^* are the upper limits of the stretch rate and the cross-bridges 'elongation'. Our tests showed that this approximation resulted in the δ values that were very close to those obtained in ODE solution of the initial non-stationary equations for the duration of the time-step for macromechanics. It should also be noted that, for the same purpose of better convergence, we used the ϑ value found in the solution of ODE system for cell-level electromechanics in T_{act} instead of its quasi-stationary approximation [31, 32].

2. A segregated numerical approximation scheme

2.1. Space discretization

The myocardial computational domain Ω is discretized using a quasi-uniform unstructured tetrahedral mesh $\mathscr{T}_{h_m}$ for cellular and three-dimensional mechanics models and $\mathscr{T}_{h_e}$ for monodomain and cellular ionic electrophysiology models, and the meshes $\mathscr{T}_{h_m}$ and $\mathscr{T}_{h_e}$ are not in any way consistent with each other. In this paper, h_m and h_e represent the corresponding mesh sizes. In all further examples, the condition $h_m \geqslant h_e$ and the condition of exact coincidence of the physical boundaries of the discretized domain $\partial\mathscr{T}_{h_m} = \partial\mathscr{T}_{h_e}$ are satisfied. Note that the space-discretization scheme of equations and intergrid interpolation operator described below allows mismatching of boundaries $\partial\mathscr{T}_{h_m}$ and $\partial\mathscr{T}_{h_e}$ at the cost of additional errors.

Let $\mathscr{V}_h^r$ be the classical Lagrange finite element space of piecewise polynomial functions $\mathscr{P}_r$ of degree at most r on a tetrahedral mesh $\mathscr{T}_h$ with set of cells $\mathscr{C}_h$, i.e., $\mathscr{V}_h^r = \{v \in H^1(\Omega) \cap C^0(\overline{\Omega}) : v|_c \in \mathscr{P}_r(c)\ \forall c \in \mathscr{C}_h\}$. Let $Q^s = \{w_q, \boldsymbol{\xi}_q\}_{q=1}^{n_q}$ be an internal positive Gaussian quadrature formula for tetrahedra of the s-th polynomial order of accuracy, i.e., for any $f \in \mathscr{P}_s(c)$ it holds $\int_c f(x)\,\mathrm{d}x = |c| \sum_{q=1}^{n_q} w_q f\left(\sum_{v=1}^4 \xi_q^v \mathbf{p}^v\right)$, where c is a tetrahedron with vertices $\{\mathbf{p}^v\}_{v=1}^4$. We denote the q-th quadrature point on a cell $c \in \mathscr{C}_h$ as $\mathbf{x}_q^c = \sum_{v=1}^4 \xi_q^v \mathbf{p}^v$ and introduce a space $\mathscr{Q}_h^s(Q^s)$ of discrete mesh functions containing one degree of freedom at each quadrature point $\mathbf{x}_q^c$ of each mesh cell. For an arbitrary $p_h \in \mathscr{Q}_h^s(Q^s)$ we denote its restriction to cell c by p_h^c and its value at the q-th quadrature point in c by $(p_h)_q^c$. Also, we denote a projection operator $I_h : C^0(\mathscr{T}_h) \to \mathscr{Q}_h^s(Q^s)$ as $(I_h p)_q^c = p(\mathbf{x}_q^c)$ for any $p \in C^0(\mathscr{T}_h)$. Finally, we use the notation

$$\fint\limits_{\mathscr{T}_h, Q^s} f(\mathbf{p}_h, \mathbf{x})\,\mathrm{d}\mathbf{x} := \sum_{c \in \mathscr{T}_h} |c| \sum_{q=1}^{n_q} w_q f\left((\mathbf{p}_h)_q^c,\ \mathbf{x}_q^c\right)$$

to denote the approximate integral for the element-wise continuous function f depending on a vector mesh-function $\mathbf{p}_h \in [\mathscr{Q}_h^s(Q^s)]^d$. To calculate efficiently projections of finite element functions defined on a mesh $\mathscr{T}_{h_1}$ onto the space of mesh functions defined at the points of quadratures on another mesh $\mathscr{T}_{h_2}$ corresponding to a quadrature formula Q^{s_2}, we use mapping $c^*_{h_2,h_1} : \mathscr{C}_{h_2} \times \{1, \ldots, n_{q,2}\} \to \mathscr{C}_{h_1}$:

$$c^*_{h_2,h_1}(c_2, q) = \arg\min_{c_1 \in \mathscr{C}_{h_1}} \left(\min_{\mathbf{y} \in c_1} ||\mathbf{y} - \mathbf{x}_q^{c_2}|| \right)$$

where $\mathscr{C}_{h_1}$ and $\mathscr{C}_{h_2}$ are sets of cells $\mathscr{T}_{h_1}$ and $\mathscr{T}_{h_2}$, and $n_{q,2}$ is the number of points in Q^{s_2}.

To solve the equations of continuous mechanics, as well as the monodomain equation, we use the finite element method, at the same time we solve the cellular equations independently at the points of the quadratures on the corresponding meshes. We describe the displacement field $\mathbf{u}$ as a continuous piecewise quadratic function $\mathbf{u}_{h_m} \in [\mathscr{V}_{h_m}^2]^3$ in the space $[\mathscr{V}_{h_m}^2]^3$ with the basis $\{\boldsymbol{\varphi}_i\}_{i=1}^{N_\mathbf{u}}$. Similarly,

we describe the transmembrane voltage v as a continuous piecewise linear function $v_{h_e} \in \mathscr{V}^1_{h_e}$ in the space $\mathscr{V}^1_{h_e}$ with the basis $\{\psi_i\}_{i=1}^{N_V}$. To calculate numerically integrals arising in weak formulations of equations of continuous mechanics and propagation of electrical activation, we use the quadrature formulas $Q^{s_m} = \{w_q, \boldsymbol{\xi}_q\}_{q=1}^{n_{q,m}}$ and $Q^{s_e} = \{w_q, \boldsymbol{\xi}_q\}_{q=1}^{n_{q,e}}$, respectively. For the sake of brevity, the spaces $\mathscr{Q}^{s_m}_{h_m}(Q^{s_m})$ and $\mathscr{Q}^{s_e}_{h_e}(Q^{s_e})$ will be denoted by $\mathscr{Q}^{s_m}_{h_m}$ and $\mathscr{Q}^{s_e}_{h_e}$, respectively. After discretization, the state variables $\mathbf{w}$ are described by mesh function $\mathbf{w}_{h_e} \in [\mathscr{Q}^{s_e}_{h_e}]^{n_w}$ on $\mathscr{T}_{h_e}$, and the state variables $\mathbf{a}$ are described by mesh functions $\mathbf{a}_{h_m} \in [\mathscr{Q}^{s_m}_{h_m}]^{n_a}$ on $\mathscr{T}_{h_m}$.

Finally, the semi-discretized formulation of the coupled problem reads: Find $\mathbf{u}_{h_m} \in [\mathscr{V}^2_{h_m}]^3$, $v_{h_e} \in \mathscr{V}^1_{h_e}$, $\mathbf{w}_{h_e} \in [\mathscr{Q}^{s_e}_{h_e}]^{n_w}$, and $\mathbf{a}_{h_m} \in [\mathscr{Q}^{s_m}_{h_m}]^{n_a}$ for any $t \in [0,T]$ such that the following equations hold:

$$\int_{\mathscr{T}_{h_m}} \rho \ddot{\mathbf{u}}_{h_m} \cdot \boldsymbol{\varphi}_i \,\mathrm{d}\mathbf{x} + \int\!\!\!\!\!\!\diagup_{\mathscr{T}_{h_m}, \mathscr{Q}^{sm}_{hm}} \mathbb{P}(\mathbb{F}_{h_m},\, \dot{\mathbb{F}}_{h_m},\, \mathbf{a}_{h_m}) : \nabla \boldsymbol{\varphi}_i \,\mathrm{d}\mathbf{x} + \int_{\partial \mathscr{T}_{h_m}} p_{\mathrm{ext}} J_{h_m} \boldsymbol{\varphi}_i \cdot \mathbb{F}^{-T}_{h_m} \mathbf{N}_{h_m} \,\mathrm{d}\mathbf{s}$$
$$+ \int_{\partial \mathscr{T}_{h_m}} [(k_{\|} \mathbf{N}_{h_m} \otimes \mathbf{N}_{h_m} + k_{\perp}(\mathbb{I} - \mathbf{N}_{h_m} \otimes \mathbf{N}_{h_m}))(\mathbf{u}_{h_m} - (\mathbf{u}_{\mathrm{spr}})_{h_m})] \cdot \boldsymbol{\varphi}_i \,\mathrm{d}\mathbf{s} = 0$$
$$\forall i \in \{1, \ldots, N_{\mathbf{u}}\}$$

$$\int\!\!\!\!\!\!\diagup_{\mathscr{T}_{h_e}, \mathscr{Q}^{se}_{he}} C_m(\mathbf{w}_{h_e})\, \dot{v}_{h_e} \psi_i \,\mathrm{d}\mathbf{x} + \int_{\mathscr{T}_{h_e}} \nabla \psi_i \cdot \sigma \nabla v_{h_e} \,\mathrm{d}\mathbf{x} + \int\!\!\!\!\!\!\diagup_{\mathscr{T}_{h_e}, \mathscr{Q}^{se}_{he}} i_{\mathrm{ion}}(v_{h_e},\, \mathbf{w}_{h_e}) \psi_i \,\mathrm{d}\mathbf{x}$$
$$= \int_{\mathscr{T}_{h_e}} i_{\mathrm{stim}} \psi_i \,\mathrm{d}\mathbf{x} \quad \forall i \in \{1, \ldots, N_v\}$$

$$(\dot{\mathbf{w}}_{h_e})^c_q = \mathbf{r}_{\mathbf{w}}(v_{h_e}(\mathbf{x}^c_q),\, (I_{h_e}\mathbb{F}_{h_m})^c_q,\, (\mathbf{w}_{h_e})^c_q) \qquad \forall q \in \{1, \ldots, n_{q,e}\}, \quad \forall c \in \mathscr{C}_{h_e}$$
$$(\dot{\mathbf{a}}_{h_m})^c_q = \mathbf{r}_{\mathbf{a}}(\mathbb{F}_{h_m}(\mathbf{x}^c_q),\, \dot{\mathbb{F}}_{h_m}(\mathbf{x}^c_q),\, (I_{h_m} v_{h_e})^c_q,\, (\mathbf{a}_{h_m})^c_q) \quad \forall q \in \{1, \ldots, n_{q,m}\}, \quad \forall c \in \mathscr{C}_{h_m}$$

where $\mathbb{F}_{h_m} = \mathbb{I} + \nabla \mathbf{u}_{h_m}$, $\dot{\mathbb{F}}_{h_m} = \nabla \dot{\mathbf{u}}_{h_m}$, $J_{h_m} = \det \mathbb{F}_{h_m}$, and $\mathbf{N}_{h_m}$ is the external unit normal to boundary of $\mathscr{T}_{h_m}$. Expression $C_m(\mathbf{w}_{h_e})$ implies the corresponding component from the vector $\mathbf{w}_{h_e}$. The intergrid projections are defined as $(I_{h_e}\mathbb{F}_{h_m})^c_q = \mathbb{I} + \sum_{i:\ \boldsymbol{\varphi}_i|_{c_m} \neq 0} [\mathbf{u}_{h_m}]_i \nabla \boldsymbol{\varphi}_i(\mathbf{x}^c_q)$, where $c_m = c^*_{h_e,h_m}(c,q)$, and $(I_{h_m} v_{h_e})^c_q = \sum_{i:\ \psi_i|_{c_e} \neq 0} [v_{h_e}]_i\, \psi_i(\mathbf{x}^c_q)$, where $c_e = c^*_{h_m,h_e}(c,q)$.

2.2. Time discretization

We use the Godunov splitting scheme [10] and iterate over time for each of the considered submodels: cellular electrophysiology, cellular mechanics, monodomain model and continuous mechanics. Similarly to [24], we use fractional time steps relative to a base time step of the continuous mechanical model $\tau_m = \Delta t$, namely,

for the monodomain model we use time step $\tau_e = \Delta t/N_e$ and the cellular models are advanced in time with step $\tau_o = \Delta t/N_o$, $N_o = k_o N_e$, where $N_e, N_o, k_o \in \mathbb{N}$.

We denote vectors of degrees of freedom for displacements and transmembrane potential using the capital letters U and V. Since the mesh functions $\mathbf{w}_{h_e}$ and $\mathbf{a}_{h_m}$ are collocated at quadrature points, we do not use special notations for the degrees of freedom of these functions. For the sake of simplicity, we drop the lower indices h_m and h_e, and move the cell index c down so that the elements of the vectors are numbered by the lower multi-index q,c. The superscript '$n+k/N_e+l/N_o$' denotes values at the moment $t^{n+k/N_e+l/N_o} = n\tau_m + k\tau_e + l\tau_o$. Starting with $n = k = l = 0$ and using these notations, we describe the process of solving equations as follows.

1. Perform k_o iterations over time to solve cellular ODEs. The ODEs are solved independently at each point of the quadrature by the CVODE package [4, 12] with a stiff solver based on backward differentiation formulas (BDFs) with order varying between 1 and 5. The first order BDF is reduced to the implicit Euler scheme:

$$\frac{\mathbf{w}_{q_e,c_e}^{n+k/N_e+(l+1)/N_o} - \mathbf{w}_{q_e,c_e}^{n+k/N_e+l/N_o}}{\tau_o} = \mathbf{r}_{\mathbf{w}}(V^{n+k/N_e},\, U^n,\, \mathbf{w}_{q_e,c_e}^{n+k/N_e+(l+1)/N_o}) \qquad \forall q_e \in \{1,\dots,n_{q,e}\}, \quad \forall c_e \in \mathscr{C}_{h_e}$$

$$\frac{\mathbf{a}_{q_m,c_m}^{n+k/N_e+(l+1)/N_o} - \mathbf{a}_{q_m,c_m}^{n+k/N_e+l/N_o}}{\tau_o} = \mathbf{r}_{\mathbf{a}}(U^n,\, \dot{U}^n,\, V^{n+k/N_e},\, \mathbf{a}_{q_m,c_m}^{n+k/N_e+(l+1)/N_o}) \qquad \forall q_m \in \{1,\dots,n_{q,m}\}, \quad \forall c_m \in \mathscr{C}_{h_m}$$

   where $\dot{U}^n$ is defined below.

2. Perform one iteration in time to solve the monodomain equation. An implicit-explicit (IMEX) scheme is used for time discretization leading to a linear problem:

$$\mathscr{M}^{C_m}(\mathbf{w}^{n+(k+1)/N_e})\dot{V}^{n+(k+1)/N_e} + \mathscr{A}^{\sigma} V^{n+(k+1)/N_e} + \mathscr{I}_{\text{ion}}(V^{n+k/N_e},\, \mathbf{w}^{n+(k+1)/N_e}) = \mathscr{I}_{\text{stim}}^{n+(k+1)/N_e}$$

   where

$$\dot{V}^{n+(k+1)/N_e} := \frac{V^{n+(k+1)/N_e} - V^{n+k/N_e}}{\tau_e}, \quad \mathscr{M}_{ij}^{C_m}(\mathbf{w}) := \int\limits_{\mathscr{T}_{h_e},\mathscr{D}_{h_e}^{se}} C_m(\mathbf{w})\; \psi_j \psi_i \,\mathrm{d}\mathbf{x}$$

$$\mathscr{A}_{ij}^{\sigma} := \int\limits_{\mathscr{T}_{h_e}} \nabla\psi_i \cdot \sigma \nabla\psi_j \,\mathrm{d}\mathbf{x}, \quad \mathscr{I}_{\text{ion,i}}(V,\, \mathbf{w}) := \int\limits_{\mathscr{T}_{h_e},\mathscr{D}_{h_e}^{se}} i_{\text{ion}}(v_{h_e}(V),\, \mathbf{w})\psi_i \,\mathrm{d}\mathbf{x}$$

$$\mathscr{I}_{\text{stim},i}^{n+(k+1)/N_e} := \int\limits_{\mathscr{T}_{h_e}} i_{\text{stim}}(t^{n+(k+1)/N_e})\; \psi_i \,\mathrm{d}\mathbf{x}$$

3. Repeat the first two steps $N_e - 1$ more times. Then, solve a nonlinear algebraic system arising from continuous mechanics equations discretized by the implicit constant acceleration scheme:

$$\mathscr{M}^{\rho}\ddot{U}^{n+1} + \mathscr{P}(U^{n+1}, \dot{U}^{n+1}, \mathbf{a}^{n+1}) + \widehat{p}(U^{n+1}) + \mathscr{G}(U^{n+1} - U^{n+1}_{\text{spr}}) = 0$$

where

$$\ddot{U}^{n+1} := \frac{U^{n+1} - 2U^n + U^{n-1}}{\tau_m^2},\ \dot{U}^{n+1} := \frac{U^{n+1} - U^n}{\tau_m},\ \mathscr{M}^{\rho}_{ij} := \int\limits_{\mathscr{T}_{h_m}} \rho\ \boldsymbol{\varphi}_i \cdot \boldsymbol{\varphi}_j \,\mathrm{d}\mathbf{x}$$

$$\mathscr{P}_i(U, \dot{U}, \mathbf{a}) := \int\limits\!\!\!\!\!\!\diagup_{\mathscr{T}_{h_m}, \mathscr{D}^{sm}_{h_m}} \mathbb{P}(\mathbb{F}_{h_m}(U),\ \dot{\mathbb{F}}_{h_m}(\dot{U}),\ \mathbf{a}) : \nabla\boldsymbol{\varphi}_i \,\mathrm{d}\mathbf{x}$$

$$\widehat{p}_i(U) := \int\limits_{\partial\mathscr{T}_{h_m}} \boldsymbol{\varphi}_i \cdot [p_{\text{ext}} J_{h_m}(U) \mathbb{F}^{-T}_{h_m}(U)] \mathbf{N}_{h_m} \,\mathrm{d}\mathbf{s}$$

$$\mathscr{G}_{ij} := \int\limits_{\partial\mathscr{T}_{h_m}} [k_{\perp}(\boldsymbol{\varphi}_i \cdot \boldsymbol{\varphi}_j) + (k_{\parallel} - k_{\perp})(\mathbf{N}_{h_m} \cdot \boldsymbol{\varphi}_i)(\mathbf{N}_{h_m} \cdot \boldsymbol{\varphi}_j)] \,\mathrm{d}\mathbf{s}$$

4. Advance in time, $n := n + 1$, repeating steps 1–3 until $t^n \geqslant T$.

The nonlinear system that arises after the discretization of the continuous mechanics equation is solved by the inexact Newton method implemented in the KinSol package [12, 13]. To solve linear systems arising at Newton steps and after discretization of the monodomain equation, we use the iterative BiCGStab solver with the second order Crout-ILU preconditioner MPT_ILUC implemented in the INMOST framework [33, 36]. The cardiac electromechanical framework CarNum [15] was used to build the overall numerical scheme, assemble the linear systems, and customize the exchanges and interactions between the individual submodels.

3. Numerical experiments

In order to investigate the impact of mesh steps in discretizing electrophysiological and mechanical processes, we consider a series of experiments on a slab geometry $\Omega = [0,\ k_x L] \times [0,\ k_y L] \times [0,\ k_z L]$, where L is a base length unit and $k_x, k_y, k_z \in \mathbb{N}$. For this geometry, we first construct a uniform cubic mesh with steps $h = L/a$, where $a \in \mathbb{N}$ is the division number. Each element of the cubic mesh is divided into 6 tetrahedra resulting in a consistent tetrahedral mesh $\mathscr{T}_h$. We add indices e and m to distinguish between parameters for electrical and mechanical parts of the problem. Unless otherwise stated, the model parameters from Table 2 are used in all experiments. To solve nonlinear systems arising from the discretization of mechanics, the relative drop of an initial residual by 10^8 times is used as a stop criterion, and for

linear systems arising from the discretization of the monodomain equation, the relative drop of an initial residual by 10^{12} times is used. The ODEs were solved using the CVODE package [4] with parameters reltol $= 10^{-6}$ and abstol $= 10^{-14}$.

3.1. Electrophysiology benchmark

First of all, we need to find out which mesh steps are necessary to reproduce correctly the electrophysiological processes solely. For this purpose, we turn off the mechanical processes by setting $\mathbf{u}(\mathbf{x},t) = 0 = \text{const}$ and perform slightly modified benchmark [20] for activation of a piece of myocardium:
Geometry: a slab with $L = 10$ mm, $k_x = 9$, $k_y = k_z = 1$;
Fibers: $\mathbf{f} = (1,0,0)^T$;
Stimulus: $i_{\text{stim}}(\mathbf{x},t) = \begin{cases} \widehat{i}_{\text{stim}}, & \mathbf{x} \in [0,\ 2.5]^3 \text{ mm},\ t \in [0,\ 20] \text{ ms} \\ 0, & \text{otherwise}, \end{cases}$
where $\widehat{i}_{\text{stim}} = 40\ \mu A/\mu F$;
Discretization: the mesh is constructed with the division number $a_e \in \{4,\dots,24\}$, the monodomain equations are discretized with the quadrature order $s_e \in \{1,\dots,5\}$, $\tau_e = \tau_o = 0.01$ ms.

As can be seen in Fig. 1, the distribution of the activation time along the slab diagonal almost coincides with deviation less than 1 ms at $a_e \geqslant 12$, i.e., $h_e = L/a_e \leqslant 0.8$ mm. In addition, it can be seen that the activation times depend mainly on the mesh step h_e rather than s_e, i.e., the higher orders of the used quadratures s_e play insignificant role. In the figure, we do not plot the graphs for $s_e > 2$ because visually the results are indistinguishable from the case $s_e = 2$. Moreover, if we consider C_m as a piecewise constant on the cell function and compute the integrals included in the mass term exactly, i.e., take $\widehat{\mathscr{M}}^{C_m}_{ij} = \int_{\mathscr{T}_{h_e}} C_m \psi_i \psi_j \, \mathrm{d}\mathbf{x}$, then for $s_e = 1$ the results also coincide visually with the case $s_e = 2$, and actually differ by no more than 0.01 ms. Thus, to simplify the calculation without significant loss in accuracy, we recommend to use the mesh step $h_e \leqslant 0.8$ mm and the mid point quadrature corresponding to $s_e = 1$.

3.2. Activation of heterogeneous tissue

In this experiment we study the influence of the choice of spatial discretization of the mechanics equation on the numerical result of activation of a heterogeneous piece of myocardium [32] (see Fig. 2):
Geometry: a slab with $L = 10$ mm, $k_x = k_y = 9$, $k_z = 1$;
Time: $t \in [0,T]$, $T = 1000$ ms;
Fibers: $\mathbf{f} = (1,0,0)^T$;
Stimulus: $i_{\text{stim}}(\mathbf{x},t) = \begin{cases} \widehat{i}_{\text{stim}} \cdot f_{\text{hat}}(t), & \mathbf{x} \in [0,\ 30] \times [0,\ 5] \times [0,\ 10] \text{ mm} \\ 0, & \text{otherwise}, \end{cases}$
where $\widehat{i}_{\text{stim}} = 25\ \mu A/\mu F$, $f_{\text{hat}}(t) = f_w\left((t - T_{\text{beg}})/t_{\text{set}}\right) - f_w\left((t - (T_{\text{end}} - t_{\text{set}}))/t_{\text{set}}\right)$,

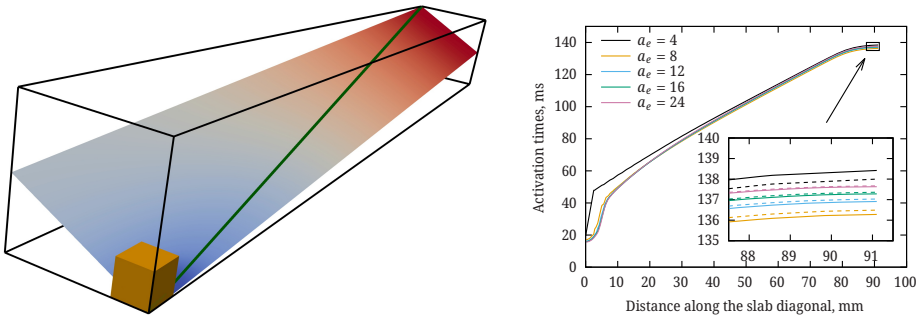

Figure 1. Left: a sketch of the electrophysiology benchmark, the stimulation region is marked in yellow, the black frames show the boundary of the computational region, and the green line shows the diagonal along which the results were plotted. Right: activation times along the diagonal of slab $90 \times 10 \times 10$ mm for meshes with step $h_e = L/a_e$, $L = 10$ mm. The results are presented for the quadrature orders $s_e = 1$ (solid line) and $s_e = 2$ (dashed line). The main window shows plots only for $s_e = 1$.

$f_w(x) = (|x| - |x-1|)/2$, and $T_{\text{beg}} = 100$ ms, $T_{\text{end}} = 103$ ms, $t_{\text{set}} = 1$ ms;
Heterogeneity is introduced through additional parameters of the Aliev–Panfilov model as

$$k_{i1}(\mathbf{x}) = \widehat{k}_{i1} f_H(x,y), \qquad k_{i2}(\mathbf{x}) = \widehat{k}_{i2} f_H(x,y)$$

$$f_H(x,y) = \begin{cases} 1, & (x,y) \in [x_1,\ x_2] \times [y_1,\ y_2] \\ 0, & (x,y) \notin [x_1 - d_x,\ x_2 + d_x] \times [y_1 - d_y,\ y_2 + d_y] \\ 1 - \frac{\rho^2(x,[x_1,x_2]) + \rho^2(y,[y_1,y_2])}{I(x \notin [x_1,x_2]) d_x^2 + I(y \notin [y_1,y_2]) d_y^2}, & \text{otherwise} \end{cases}$$

where $\rho(x,[x_1,x_2]) = \min_{y \in [x_1,x_2]} |y - x|$, $I(\cdot)$ is an indicator function, $x_1 = 27$ mm, $x_2 = 36$ mm, $y_1 = 0$ mm, $y_2 = 36$ mm, $d_x = 1.35$ mm, $d_y = 3.6$ mm, $\widehat{k}_{i1} = 5$ and $\widehat{k}_{i2} = 2$. Physically, this corresponds to a tissue sample having a region with an increased excitation threshold and an increased outward currents of positive ions through the cell membrane preventing the tissue excitation and reducing its conductivity. The region also has a 'grey' zone within which the properties change gradually.
Pressure: $p_{\text{ext}} = \widehat{p} \min(1, t/T_p) I(\mathbf{x} \in \Gamma_r)$, where $\Gamma_r = \{90\} \times [0,\ 90] \times [0,10]$ mm, $\widehat{p} = 1$ kPa, $T_p = 100$ ms.
Spring fastening is applied on three boundaries

1. on $\Gamma_l = \{0\} \times [0,\ 90] \times [0,10]$ we set $k_\perp = k_\parallel = 20$ kPa, $\mathbf{u}_{\text{spr}} = 0$.
2. on $\Gamma_b = [0,\ 90] \times \{0\} \times [0,10]$ we set $k_\perp = 20$ kPa, $k_\parallel = 0$ kPa, $\mathbf{u}_{\text{spr}} = 0$.
3. on $\Gamma_r = \{90\} \times [0,\ 90] \times [0,10]$ we impose the condition of spring fastening starting from the moment $t = T_p = 100$ ms considering the springs at that moment not loaded, in other words, we set the relaxed state as $\mathbf{u}_{\text{spr}}(\mathbf{X},t) = \mathbf{u}(\mathbf{X},T_p) I(t \geqslant T_p)$ and stiffness $k_\perp = k_\parallel = 20 I(t \geqslant T_p)$ kPa.

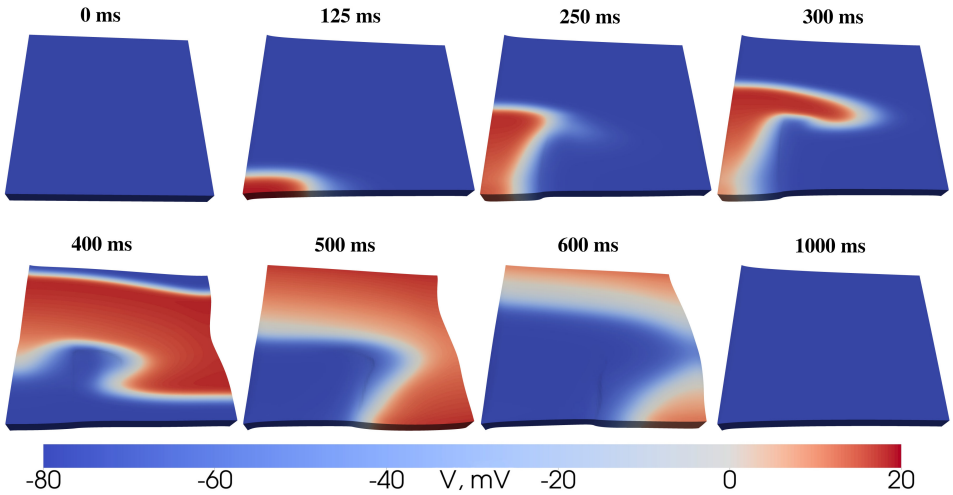

Figure 2. Propagation of transmembrane potential v in the experiment with heterogeneous myocardium activation.

Discretization: we consider a number of cases with different division numbers $a_e \in \{10,\ 12\}$, $a_m \in \{2,\dots,12\}$, and different time steps, with τ_m varying from 0.1 ms to 1 ms, and τ_e varying from 0.01 ms up to 1 ms. The time step for cellular models is fixed to $\tau_o = 0.01$ ms. For all calculations except the reference one (to be defined below), the quadrature orders $s_m = 3$ and $s_e = 1$ are used.
Method of comparison: to compare and analyze the results obtained on different grids, we consider the values of $\mathbf{u}$, v and λ_f at five points $\mathbf{p}_i = \{15i, 15i, 10i/3\},\ i \in \{1,\dots,5\}$ lying on the main diagonal of the slab, with the point $\mathbf{p}_2$ lying in the region of the material heterogeneity. The numerical solution obtained on a common tetrahedral mesh $a_m = a_e = 12$ with the discretization parameters $s_m = s_e = 5$, $\tau_m = 0.1$ ms, $\tau_e = \tau_o = 0.01$ ms is chosen to be the reference solution. To assess the numerical error of the solutions, we considered the absolute value of the deviation of the variables

$$\varepsilon_{\text{var}}(t) = \max_{i\in\{1,\dots,5\}} ||\text{var}(\mathbf{p}_i,t) - \text{var}^{\text{ref}}(\mathbf{p}_i,t)||, \quad \text{var} \in \{\mathbf{u},\ v,\ \lambda_f\}$$

where the upper index 'ref' indicates the corresponding variable of the reference solution. Also, to demonstrate the magnitude of the phase errors for all the considered cases at all five points, we calculated the moment of activation

$$t_{\text{act}} = \min\{t > T_p :\ v(t) = 0\}$$

and the moment of contraction

$$t_{\text{contr}} = \min\{t > T_p :\ \lambda_f(t) = \lambda_f^*\}$$

where $\lambda_f^* = \frac{1}{5}\sum_{i=1}^{5} (\lambda_f^{\text{ref}}(\mathbf{p}_i,T) + \lambda_f^{\text{ref}}(\mathbf{p}_i,0))/2 \approx 1.06382$.

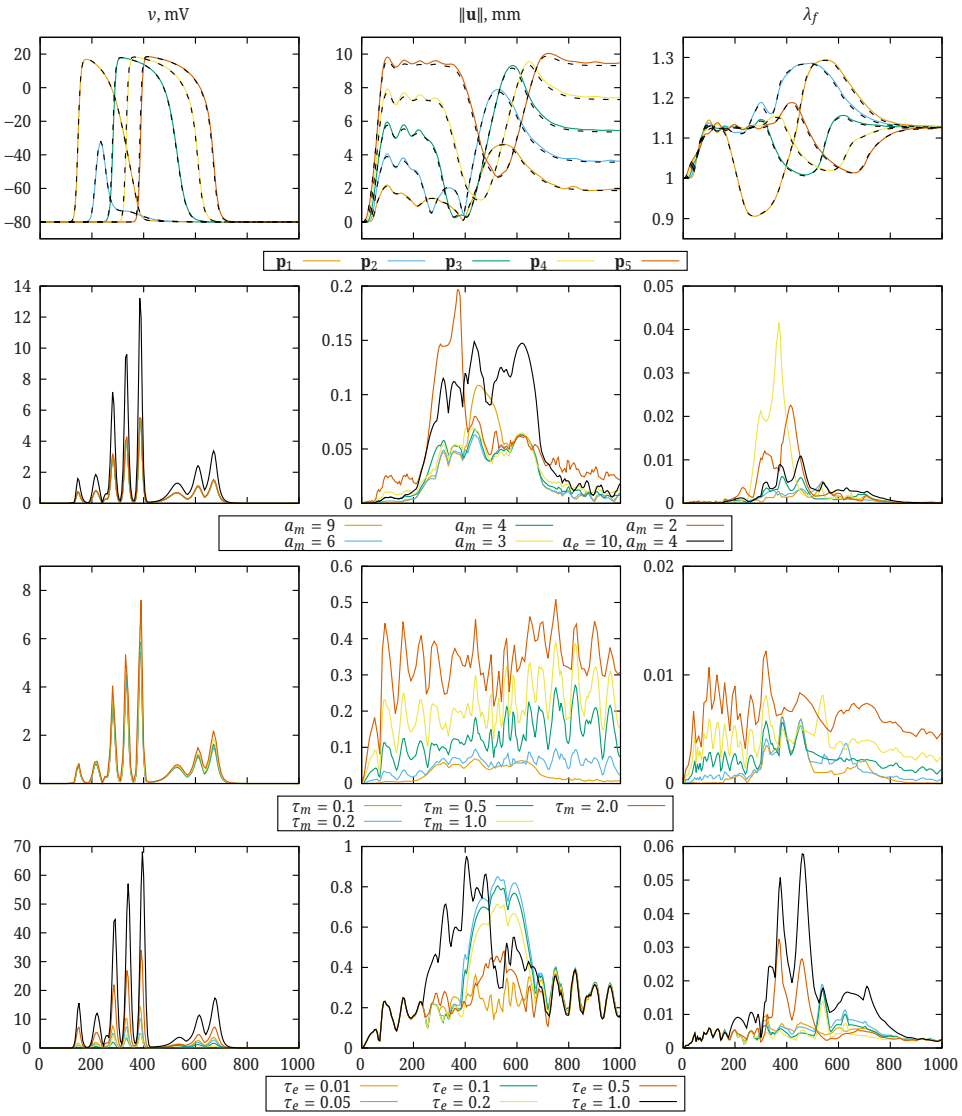

Figure 3. Plots of values and their deviations from the reference solution for the transmembrane potential v (first column), displacement $\mathbf{u}$ (second column), and fiber stretch λ_f (third column). The first row shows the evolution of the considered quantities calculated at five points $\mathbf{p}_1, \ldots, \mathbf{p}_5$, with the solid lines corresponding to the reference solution and the dashed lines corresponding to the case $a_e = 10$, $a_m = 4$, $\tau_m = 1$, $\tau_e = 0.01$. The second row shows the deviation values from the reference solution ε_v, $\varepsilon_{\mathbf{u}}$, and ε_{λ_f} for different values of a_m at fixed $a_e = 12$, $\tau_e = 0.01, \tau_m = 0.1$. The third line shows the deviation values ε_v, $\varepsilon_{\mathbf{u}}$, and ε_{λ_f} for different values of τ_m when $a_e = 12$, $a_m = 4$, $\tau_e = 0.01$ are fixed. The fourth row shows the deviation values ε_v, $\varepsilon_{\mathbf{u}}$, and ε_{λ_f} for different values of τ_e when $a_e = 10$, $a_m = 4$, $\tau_m = 1$ are fixed. Plots have the same horizontal axis showing time t in ms as in the fourth row.

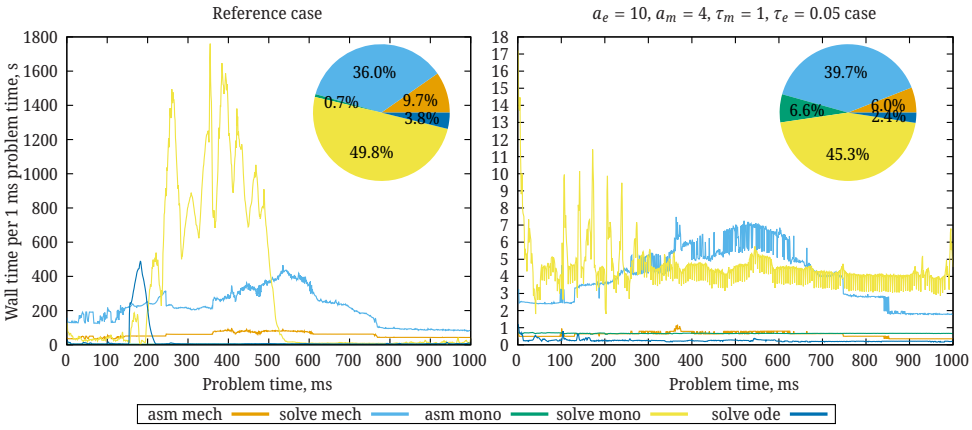

Figure 4. The wall time of computations per 1 ms in the numerical experiment with heterogeneous myocardium for separate stages: assembling of Jacobians and residuals for mechanics and monodomain, solution of arising linear and nonlinear algebraic systems, and solution of cellular ODEs. The vertical axis shows the wall time of computations in seconds, and the horizontal axis shows the number of ms of the numerical experiment. The pie chart depicts the contribution of each step to the total computation time. On the left panel: results for the reference case, for which the total computation time was 165 hours on 512 cores. On the right panel: results for the case $a_e = 10$, $a_m = 4$, $\tau_m = 1$ ms, $\tau_e = 0.05$ ms, the total computation time for which was 3 hours on 156 cores. The computations were obtained on a high performance computing cluster at Sechenov University equipped with Intel(R) Xeon(R) Gold 6230R CPUs @ 2.10GHz.

First of all, we want to understand how large can be a mesh size for the mechanical part of the problem. To this end, we performed a number of experiments with fixed $a_e = 12$ and a_m varying from 9 to 2 and present the results in the second row of Fig. 3. Large error spikes for v occur at times when this quantity changes most rapidly at some points $\mathbf{p}_i$, and are caused by phase errors. This can also be seen in the first row of Fig. 3, where the solid line shows the reference solution and the dashed line shows the solution for $a_e = 10$, $a_m = 4$, $\tau_m = 1$ ms. Although the difference of the solutions in the second row reaches 13 mV, nevertheless the plots for v visually coincide in the first row. Passing from $a_m = 4$ to $a_m = 3$ increases sharply the error in the stretch ε_{λ_f} from about 0.005 to 0.04, that is very significant since $|\lambda_f - 1| < 0.3$. As can be seen in the first row, this error is contributed mainly by the point belonging to the inhomogeneity region. This is probably due to the fact that the inhomogeneity region is poorly resolved on the coarse mesh $\mathcal{T}_{h_m}$. At the same time, the absolute displacement errors $\varepsilon_{\mathbf{u}}$ remain moderate even at $a_m = 3$. In general, it can be concluded that using $a_m = 4$, i.e., $h_m \leqslant 2.5$ mm, is sufficient to obtain reasonable accuracy.

Next, we investigate the effect of τ_m on the quality of the solutions. We performed a series of experiments with different values of τ_m and fixed $a_e = 12$, $a_m = 4$, $\tau_e = 0.01$ ms. The third row of Fig. 3 shows that an increase of τ_m from 0.1 to 1 leads to approximately linear increase in the error for $\mathbf{u}$ from 0.05 to 0.4 mm. In contrast, the effect of increasing τ_m on v and λ_f was mainly phase-specific and, as

Table 1. Activation and contraction times in a numerical experiment with a heterogeneous piece of myocardium at different discretization parameters. The first part of the table shows the activation and contraction times obtained in the reference calculation. The second part of the table shows the deviations of the times from the reference values $\Delta t_{\text{act}} = t_{\text{act}} - t_{\text{act}}^{\text{ref}}$, $\Delta t_{\text{contr}} = t_{\text{contr}} - t_{\text{contr}}^{\text{ref}}$. All times in the table are in milliseconds. Values at point $\mathbf{p}_2$ are not shown because the activation and contraction criteria were not met at this point.

case \ point				$\mathbf{p}_1$		$\mathbf{p}_3$		$\mathbf{p}_4$		$\mathbf{p}_5$	
a_e	a_m	τ_m	τ_e	t_{act}	t_{contr}	t_{act}	t_{contr}	t_{act}	t_{contr}	t_{act}	t_{contr}
12	12	0.1	0.01	154.473	185.206	289.248	363.155	340.603	451.565	394.210	535.809
a_e	a_m	τ_m	τ_e	Δt_{act}	Δt_{contr}	Δt_{act}	Δt_{contr}	Δt_{act}	Δt_{contr}	Δt_{act}	Δt_{contr}
12	9	0.1	0.01	−0.136	−0.098	−0.554	−0.734	−0.893	−1.475	−0.827	−0.964
12	6	0.1	0.01	−0.137	−0.119	−0.558	−0.725	−0.896	−0.939	−0.832	−1.347
12	4	0.1	0.01	−0.137	−0.174	−0.562	−1.011	−0.900	−1.416	−0.837	−0.206
12	3	0.1	0.01	−0.139	−0.159	−0.567	−1.253	−0.906	−1.030	−0.846	−1.754
12	2	0.1	0.01	−0.142	−0.375	−0.586	0.122	−0.926	−2.235	−0.872	−1.286
12	4	0.2	0.01	−0.139	−0.203	−0.573	−1.224	−0.915	−0.940	−0.861	−2.333
12	4	0.5	0.01	−0.144	−0.303	−0.605	−1.748	−0.958	−2.243	−0.932	−3.090
12	4	1.0	0.01	−0.152	−0.516	−0.659	−2.413	−1.028	−3.420	−1.047	−4.745
12	4	2.0	0.01	1.176	−1.179	−0.500	−4.041	−1.091	−5.540	−0.061	−7.188
10	4	0.1	0.01	−0.312	−0.251	−1.383	−2.074	−1.837	−2.374	−2.225	−3.319
10	4	1.0	0.01	−0.326	−0.605	−1.490	−3.623	−1.977	−4.718	−2.483	−5.653
10	4	1.0	0.05	−0.185	−0.445	−0.973	−3.069	−1.438	−2.690	−1.682	−4.951
10	4	1.0	0.10	−0.011	−0.243	−0.373	−2.205	−0.805	−1.871	−0.808	−3.831
10	4	1.0	0.20	0.327	0.072	0.728	−0.681	1.072	−0.089	0.689	−1.965
10	4	1.0	0.50	1.809	1.185	4.918	3.937	5.692	4.810	6.266	3.996
10	4	1.0	1.00	3.865	2.653	11.305	11.819	13.210	12.712	15.117	12.964

can be seen in Table 1, led mainly to a small decrease in the activation and contraction times. Assuming that the relative (compared with the reference solution) errors of activation and contraction front propagation velocities can be estimated as $(t_{\text{act}} - t_{\text{act}}^{\text{ref}})/(t_{\text{act}}^{\text{ref}} - T_p)$, where $T_p = 100$ ms is the start of stimulation time, we can say that during the increase in τ_m from 0.1 to 1 ms, the activation and excitation front propagation velocity increased by approximately 0.7%. The phase error at $\tau_m = 2$ ms differs from all other cases and is expressed in the slowing down of the front propagation. This is probably caused by the fact that at such large step certain nonlinear effects are reproduced incorrectly. In general, we conclude that if an error in the front propagation velocity of the order of 1% is acceptable, we can use the time step $\tau_m = 1$ ms for mechanics.

Finally, we vary τ_e at fixed $a_e = 10$, $a_m = 4$, $\tau_m = 1$ ms. For all quantities investigated, the error in changing τ_e from 0.01 to 1 ms is mainly phase-related. As expected, increasing τ_e leads to slower front propagation, rf. Table 1. However, as can be seen in the fourth row of Fig. 3 and Table 1, as the step τ_e increases from 0.01 to 1, the modulus of the error first drops and only then increases. This unexpected result is due to the fact that phase errors caused by time discretization for mechanics and electrophysiology have opposite signs and thus there is such a relation between τ_e and τ_m, at which the arising phase errors are mutually compensated. This is observed at τ_e between 0.1 and 0.3 ms.

We also measured the computation times for separate stages: assembling of linear systems for mechanics and monodomain, solving these linear systems while

Table 2. The parameters of submodels (two left panels) and initial conditions of state variables (right panel) are given by default, i.e., used in numerical experiments if other values were not explicitly specified when setting them up. For the active stress model (middle panel), only those parameters whose values differed from those presented in [31, Table 1] are given.

Models		
Monodomain model		
σ_{iso}	0.5	mm^2/ms
σ_{aniso}	4.5	mm^2/ms
Membrane capacitance C_m		
k_m	10^{-3}	ms^{-1}
K_m	2.5	—
Aliev–Panfilov model		
V_{min}	-80	mV
V_{norm}	100	mV
τ	12.9	ms
μ_1	0.2	—
μ_2	0.3	—
k	8	—
a	0.1	—
k_{i1}	0	—
k_{i2}	0	—
Mechanical model		
ρ	1	mg/mm^3
μ	0.55	kPa
b	2.85	—
K	50	kPa
Titin elastic model		
t_{tit}	1.0297	kPa
q_1	37.02159500	—
q_2	-257.47066444	—
q_2^*	772.41199331	—
q_3	556.32176365	—

Active stress model		
l_{s0}	$1.90 \cdot 10^{-3}$	mm
l_0	$1.30 \cdot 10^{-3}$	mm
l_m	$1.63 \cdot 10^{-3}$	mm
l_z	$0.035 \cdot 10^{-3}$	mm
l_a	$1.12 \cdot 10^{-3}$	mm
l_b	$0.16 \cdot 10^{-3}$	mm
p_{f1}	0.5	—
E	$2.5 \cdot 10^{-3}$	mN/mm
N_m	$283 \cdot 10^6$	mm^{-2}
N_{xb}	150	—
h	10^{-5}	mm
k_{cb}	$75 \cdot 10^{-3}$	ms^{-1}
k_{21}	20	—
γ	4	—
δ^*	0.4	—
δ_2^*	0.37	—
a_{10}	1.5	—
b_{10}	8.5	—
B_{cyt}	130	μM
G_{xfer}	$3.8 \cdot 10^{-3}$	ms^{-1}
G_{leak}	$3 \cdot 10^{-5}$	ms^{-1}
k_{NCX}	0.8	—
k_4	$2.5 \cdot 10^{-4}$	ms^{-1}
K_2	125	—
K_R	200	μM

Initial conditions		
Monodomain state		
v	-80	mV
Membrane capacitance		
C_m	1	—
AP states		
ν	0.02	—
Mechanical states		
$\mathbf{u}$	$\mathbf{0}$	mm
$\partial_t \mathbf{u}$	$\mathbf{0}$	mm/ms
Active stress states		
n	10^{-6}	—
A_1	0.018	—
A_2	0.018	—
c	0.078	μM
c_{SS}	0.080	μM
c_{SR}	616	μM
p	0.37	—
R	0.265	—
ϑ	0.5	—

dealing with linear or nonlinear algebraic problems, and solving cellular ODEs. In Fig. 4, we present the corresponding results for the reference case and the case with $a_e = 10$, $a_m = 4$, $\tau_m = 1$, $\tau_e = 0.05$, with the total time for the former and latter computations being approximately 165h on 512 cores and 3h on 156 cores, respectively. It is noteworthy that the difference in the rate of propagation of the activation front between the solutions does not exceed 1.2%, and the difference in the actual values of v, $\mathbf{u}$, and λ_f is noticeable only in the region where myocardial properties change dramatically. In other words, for practical calculations it is not necessary to perform such heavy computations as were done to obtain the reference solution, but it is enough to use much coarser discretization with $a_e = 10$, $a_m = 4$, $\tau_m = 1$, $\tau_e = 0.05$. Note that in this work we did not seek to minimize the computation time and did not make special adjustments of preconditioners and other tunings, so the presented data on wall time serve only for demonstration and can be improved.

4. Conclusions

In this paper, we presented the fully temporally and spatially segregated scheme for solving coupled electromechanical cardiac problems, including the submodels of cellular electrophysiology and mechanics, as well as the monodomain submodel

of transmembrane potential propagation and the submodel of continuous three-dimensional mechanics. The proposed numerical scheme couples electrical and mechanical parts through the state variables at the integration points on two separate unstructured tetrahedral meshes without the need for interpolations from one mesh to another. Analyzing our discretization scheme for the monodomain equation on the well-known electrophysiological benchmark [20], we found that a mesh step of $h_e \leqslant 0.8 \sim 1$ mm is optimal from the point of view of solution accuracy. Further, we analyzed the impact of spatial discretization resolution for the mechanical part of the equations and temporal discretization resolution for both mechanical and monodomain equations on the electromechanical problem with inhomogeneous myocardial slab [32]. We found that the mesh step $h_m \leqslant 2.5$ mm can be used with reasonable accuracy for the spatial discretization of the mechanical part. We also found that the time discretization of both the mechanical equations and the monodomain equation leads mainly to phase errors with opposite signs, which can be exploited for mutual suppression of errors. Finally, we have considered two examples of calculations and demonstrated how the use of the proposed segregated numerical scheme can speed up the calculations compared to the conventional scheme using a common mesh for the monodomain equation and mechanics: the speed-up factor 10^1–10^2 with a relatively small loss of accuracy is obtained.

Acknowledgement: The parallel numerical experiments were conducted on the HPC system of the Institute for Computer Science and Mathematical Modeling, Sechenov University. Authors acknowledge colleagues from Marchuk Institute of Numerical Mathematics, Russian Academy of Sciences, and Sirius University of Science and Technology for valuable discussions about INMOST framework and numerical methods.

References

1. R. R. Aliev and A. V. Panfilov, A simple two-variable model of cardiac excitation. *Chaos, Solitons & Fractals* **7** (1996), No.3, 293–301.

2. M. Bucelli, A. Zingaro, P. C. Africa, I. Fumagalli, L. Ded, and A. Quarteroni, A mathematical model that integrates cardiac electrophysiology, mechanics, and fluid dynamics: Application to the human left heart. *International Journal for Numerical Methods in Biomedical Engineering* **39** (2023), No. 3, e3678.

3. D. Chapelle, M. A. Fernández, J.-F. Gerbeau, P. Moireau, J. Sainte-Marie, and N. Zemzemi, Numerical simulation of the electromechanical activity of the heart. In: *Functional Imaging and Modeling of the Heart: 5th International Conference, FIMH 2009, Nice, France, June 3-5, 2009. Proceedings 5*. Springer, 2009, pp. 357–365.

4. S. D. Cohen, A. C. Hindmarsh, and P. F. Dubois, CVODE, a stiff/nonstiff ODE solver in C. *Computers in Physics* **10** (1996), No. 2, 138–143.

5. F. Del Bianco, P. C. Franzone, S. Scacchi, and L. Fassina, Electromechanical effects of concentric hypertrophy on the left ventricle: a simulation study. *Computers in Biology and Medicine* **99** (2018), 236–256.

6. A. DeSimone, B. Perthame, A. Quarteroni, L. Truskinovsky, L. Ded, A. Gerbi, and A. Quarteroni, Segregated algorithms for the numerical simulation of cardiac electromechanics in the left human ventricle. In: *The Mathematics of Mechanobiology, Cetraro, Italy 2018*, 2020, pp. 81–116.

7. A. Dokuchaev, T. Chumarnaya, A. Bazhutina, S. Khamzin, V. Lebedeva, T. Lyubimtseva, S. Zubarev, D. Lebedev, and O. Solovyova, Combination of personalized computational modeling and machine learning for optimization of left ventricular pacing site in cardiac resynchronization therapy. *Frontiers in Physiology* **14** (2023): 1162520.

8. J. Fröhlich, T. Gerach, J. Krauß, A. Loewe, L. Stengel, and C. Wieners, Numerical evaluation of elasto-mechanical and visco-elastic electro-mechanical models of the human heart. *GAMM-Mitteilungen* **46** (2024), No. 3-4, e202370010.

9. Y.-C. B. Fung, Biorheology of soft tissues. *Biorheology* **10** (1973), No. 2, 139–155.

10. S. Godounov, A difference method for numerical calculation of discontinuous solutions of the equation of hydrodynamics. *Matematicheskii Sbornik* **47** (1959), No. 89-3, 271–306.

11. S. Gktepe and E. Kuhl, Computational modeling of cardiac electrophysiology: A novel finite element approach. *International Journal for Numerical Methods in Engineering* **79** (2009), No. 2, 156–178.

12. A. C. Hindmarsh, P. N. Brown, K. E. Grant, S. L. Lee, R. Serban, D. E. Shumaker, and C. S. Woodward, SUNDIALS: Suite of nonlinear and differential/algebraic equation solvers. *ACM Transactions on Mathematical Software (TOMS)* **31** (2005), No. 3, 363–396.

13. A. C. Hindmarsh, R. Serban, C. J. Balos, D. J. Gardner, D. R. Reynolds, and C. S. Woodward, User documentation for KINSOL v5.7.0 (SUNDIALS v5.7.0). Tech. Report UCRL-SM-208116, 2021.

14. P. Lamata, A. Cookson, and N. Smith, Clinical diagnostic biomarkers from the personalization of computational models of cardiac physiology. *Annals of Biomedical Engineering* **44** (2016), 46–57.

15. A. A. Liogky, A. Y. Chernyshenko, A. A. Danilov, and F. A. Syomin, CarNum: parallel numerical framework for computational cardiac electromechanics. *Russian Journal of Numerical Analysis and Mathematical Modelling* **38** (2023), No. 3, 127–144.

16. J. F. Marko and E. D. Siggia, Statistical mechanics of supercoiled DNA. *Phys. Rev. E* **52** (1995), 2912–2938.

17. C. Mendonca Costa, G. Plank, C. A. Rinaldi, S. A. Niederer, and M. J. Bishop, Modeling the electrophysiological properties of the infarct border zone. *Frontiers in Physiology* **9** (2018), 356.

18. M. P. Nash and A. V. Panfilov, Electromechanical model of excitable tissue to study reentrant cardiac arrhythmias. *Progress in Biophysics and Molecular Biology* **9** (2018), 356.

19. D. Nickerson, N. Smith, and P. Hunter, New developments in a strongly coupled cardiac electromechanical model. *EP Europace* **7** (2005), No. s2, S118–S127.

20. S. A. Niederer, E. Kerfoot, A. P. Benson, M. O. Bernabeu, O. Bernus, C. Bradley, E. M. Cherry, R. Clayton, F. H. Fenton, A. Garny, E. Heidenreich, S. Land, M. Maleckar, P. Pathmanathan, G. Plank, J. F. Rodr´iguez, I. Roy, F. B. Sachse, G. Seemann, O. Skavhaug, and N. P. Smith, Verification of cardiac tissue electrophysiology simulators using an *N*-version benchmark. *Philosophical Transactions of the Royal Society A: Mathematical, Physical and Engineering Sciences* **369** (2011), No. 1954, 4331–4351.

21. D. Nordsletten, S. Niederer, M. Nash, P. Hunter, and N. Smith, Coupling multi-physics models to cardiac mechanics. *Progress in Biophysics and Molecular Biology* **104** (2011), No. 1, 77–88.

22. P. Pathmanathan and J. P. Whiteley, A numerical method for cardiac mechanoelectric simulations. *Annals of Biomedical Engineering* **37** (2009), No. 5, 860–873.

23. F. Regazzoni and A. Quarteroni, An oscillation-free fully staggered algorithm for velocity-dependent active models of cardiac mechanics. *Computer Methods in Applied Mechanics and Engineering* **373** (2021), 113506.

24. F. Regazzoni, M. Salvador, P. Africa, M. Fedele, L. Ded, and A. Quarteroni, A cardiac electromechanical model coupled with a lumped-parameter model for closed-loop blood circulation. *Journal of Computational Physics* **457** (2022), 111083.

25. F. B. Sachse, *Computational Cardiology: Modeling of Anatomy, Electrophysiology, and Mechanics*. Springer Science & Business Media, Vol. 2966, 2004.

26. J. Sainte-Marie, D. Chapelle, R. Cimrman, and M. Sorine, Modeling and estimation of the cardiac electromechanical activity. *Computers & Structures* **84** (2006). No. 28, 1743–1759.

27. M. Salvador, L. Ded, and A. Quarteroni, An intergrid transfer operator using radial basis functions with application to cardiac electromechanics. *Computational Mechanics* **66** (2020), No. 2, 491–511.

28. M. Salvador, M. Fedele, P. C. Africa, E. Sung, A. Prakosa, J. Chrispin, N. Trayanova, A. Quarteroni, et al., Electromechanical modeling of human ventricles with ischemic cardiomyopathy: numerical simulations in sinus rhythm and under arrhythmia. *Computers in Biology and Medicine* **136** (2021), 104674.

29. F. Syomin, A simple kinetic model of myocardium contraction: calcium-mechanics coupling. *Biophysics* **59** (2014), 772–779.

30. F. A. Syomin and A. K. Tsaturyan, A simple model of cardiac muscle for multiscale simulation: passive mechanics, crossbridge kinetics and calcium regulation. *J. Theor. Biol.* **420** (2017), 105–116.

31. F. Syomin, A. Osepyan, and A. Tsaturyan, Computationally efficient model of myocardial electromechanics for multiscale simulations. *PLoS One* **16** (2021), No. 7, e0255027.

32. F. A. Syomin, V. A. Galushka, and A. K. Tsaturyan, Effect of strain-dependent conduction slowing on the re-entry formation and maintenance in cardiac muscle: 2D computer simulation. *International Journal for Numerical Methods in Biomedical Engineering* **39** (2023), No. 11, e3676.

33. K. M. Terekhov, A. Danilov, I. Konshin, and Y. Vassilevski, INMOST—a toolkit for distributed mathematical modeling. `http://www.inmost.org`

34. N. A. Trayanova, J. Constantino, and V. Gurev, Electromechanical models of the ventricles. *American Journal of Physiology-Heart and Circulatory Physiology* **301** (2011), No. 2, H279–H286.

35. N. A. Trayanova and K. C. Chang, How computer simulations of the human heart can improve anti-arrhythmia therapy. *The Journal of Physiology* **594** (2016), No. 9, 2483–2502.

36. Y. Vassilevski, K. Terechov, K. Nikitin, and I. Kapyrin, *Parallel Finite Volume Computation on General Meshes*. Springer International Publishing, Cham, 2020.

37. Z. J. Wang, A. Santiago, X. Zhou, L. Wang, F. Margara, F. Levrero-Florencio, A. Das, C. Kelly, E. Dall'Armellina, M. Vazquez, et al., Human biventricular electromechanical simulations on the progression of electrocardiographic and mechanical abnormalities in post-myocardial infarction. *EP Europace* **23** (2021), Supplement 1, i143–i152.